


# Stochastic Dynamics of a Ferromagnetic Vortex Revealed by Single-Spin Magnetometry

R. Badea, E. Haber, and J. Berezovsky\*

*Department of Physics, Case Western Reserve University, Cleveland, Ohio 44106, USA*

 (Received 24 May 2018; revised manuscript received 10 September 2018; published 13 December 2018)

We study the dynamics of a magnetic vortex in a permalloy disk, as it is switched between bistable pinning sites in the presence of room-temperature thermal noise. We use static and time-resolved magneto-optical Kerr-effect microscopy to characterize the equilibrium and nonequilibrium motion of the vortex in response to a train of magnetic field pulses. The limitations of this approach due to inhomogeneous averaging are overcome by using a proximal nitrogen-vacancy spin in diamond to probe the final position of the vortex core following a single magnetic field pulse. Repeating this single-shot measurement, we characterize the probability of switching between two bistable pinning sites as a function of pulse time. We develop a simple model of the stochastic vortex trajectory through the pinning sites' basins of attraction to understand how the separate contributions of damping and dephasing result in the observed switching behavior.

DOI: [10.1103/PhysRevApplied.10.064031](https://doi.org/10.1103/PhysRevApplied.10.064031)

## I. INTRODUCTION

Fast reliable manipulation of ferromagnetic (FM) textures such as domain walls, vortices, and skyrmions in the presence of thermal noise is necessary to realize proposed technologies in spin-based data storage, logic, sensing, and quantum information [1–5]. The vortex state in micromagnets has attracted attention, with potential applications in magnetic information transfer [6,7], magnetic logic [8], microwave amplification [9], and sensing [10]. Currently, emerging applications in magnetic recording based on moving domain walls or skyrmions in a magnetic nanowire are of intense interest.

The relaxation process of magnetic structures after excitation of dynamic modes is dominated by fast precessional motion and much slower energy dissipation bringing the system into equilibrium. In the presence of multistable equilibria and thermal fluctuations that perturb the magnetization configuration, the large difference in the time scales at work results in a nondeterministic evolution of the magnetic state. This phenomenon has previously been studied for magnetization reversal of uniformly magnetized magnetic bits [11], and the understanding of these effects allows for precessional switching of a bit using pulses faster than the relaxation time [12]. Here, we study this effect in the case of switching not of an entire magnetic structure but of the position of a nanoscale vortex core within a larger structure. The results and techniques we

present here are likely to generalize well to both skyrmions and vortex domain walls in nanowires.

A vortex state in a thin FM disk is characterized by a curl of in-plane magnetization circulating about a central core with a diameter of approximately 10 nm where the magnetization orients out of plane [see Fig. 1(a)]. The nanoscale core can be translated through the material using electric current [13] or small magnetic fields [14]. The small size of the core and the dynamics with a characteristic frequency  $> 100$  MHz lead to proposed applications with high spatial resolution or density and fast operation. However, several problems stand in the way of these future devices. First, the fast dynamics of the vortex exhibit a relatively long relaxation time (approximately 100 ns), which limits the ability to perform fast operations [15]. Second, thermal fluctuations influence the dynamics of the vortex, resulting in stochastic nondeterministic behavior [16]. Third, defects in the magnetic material cause pinning of the vortex core [17], complicating precise control of the vortex as it moves through a random pinning landscape [18]. Here, we combine time-resolved magneto-optical Kerr-effect (MOKE) microscopy with single-spin magnetometry to reveal the stochastic dynamics of a ferromagnetic vortex as it switches between two adjacent bistable pinning sites.

Our combined techniques uncover information about the dynamics that are typically obscured by inhomogeneous averaging. Vortex dynamics have been previously studied using time-resolved MOKE [15] or x-ray microscopy [19] that rely on a pulsed probe synchronized with the vortex excitation. Optical or x-ray techniques can both provide

\*jab298@case.edu

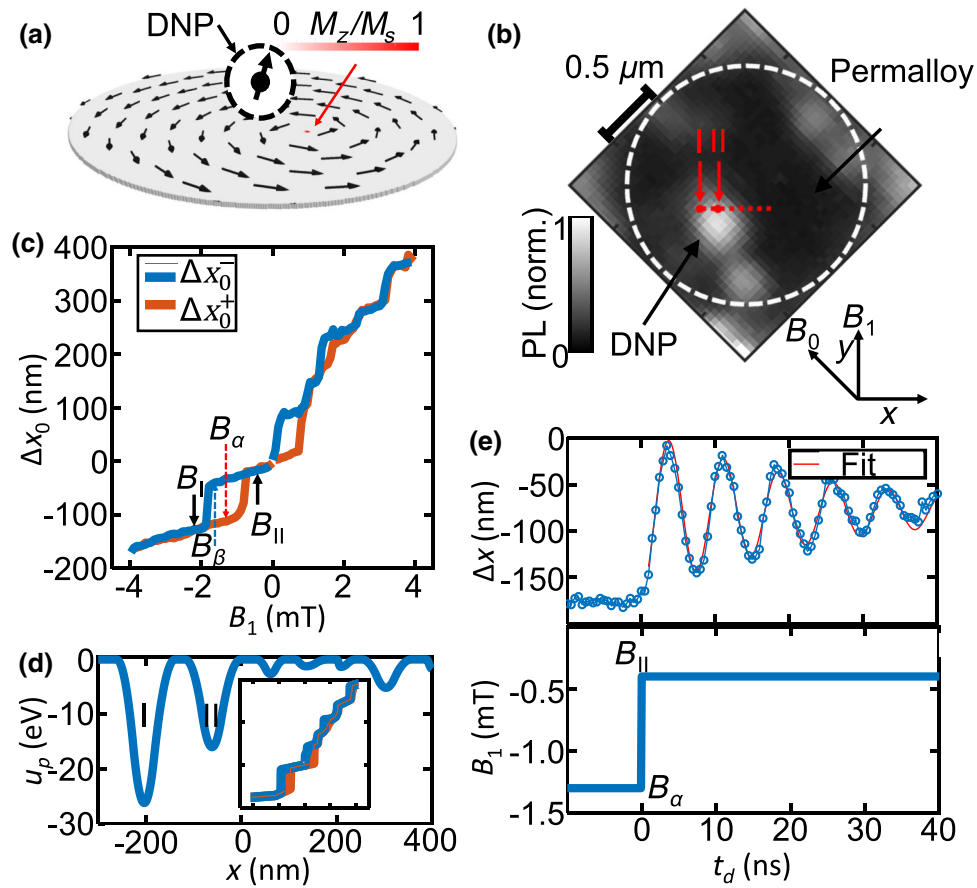


FIG. 1. (a) A simulated image of the vortex state, with the magnetization  $\mathbf{M}$  indicated by black arrows and the out-of-plane component  $M_z/M_s$  shown with the color scale. The red arrow indicates the vortex core. A diamond nanoparticle (DNP) sits atop the disk. (b) The photoluminescence map of the N-V-vortex system. The edges of the permalloy disk are illustrated by a  $2\ \mu\text{m}$  dashed circle. The path taken by the vortex core  $\Delta x_0(B_1)$  at  $B_0 = -2.8\ \text{mT}$  is illustrated by a red dotted line along with the positions of pinning sites I and II. (c) The hysteretic response  $\Delta x_0(B_1)$  for ascending (red) and descending (blue)  $B_1$ . The switching fields  $B_I = -2.2\ \text{mT}$  and  $B_{II} = -0.4\ \text{mT}$  are illustrated by black arrows while the bistable fields  $B_\alpha = -1.3\ \text{mT}$  and  $B_\beta = -1.6\ \text{mT}$  are illustrated by red and blue arrows, respectively. (d) The one-dimensional effective pinning potential  $u_p(x)$ , on the same scale as Fig. 1(c). Included in the inset is a simulated  $\Delta x_0$  in the presence of  $u_p$ , on the same scale as Fig. 1(c). (e) The nonequilibrium displacement of the vortex core  $\Delta x$  in response to a magnetic field step illustrated below, with a decaying sinusoidal fit.

time resolution much faster than the typical nanosecond-scale dynamics here, and diffraction-limited imaging resolution (100 nm and 10 nm, respectively). In a differential measurement, changes in displacement of the vortex core can be measured below the diffraction limit as the core translates within the probe spot, with resolution typically observed down to about 10 nm in optical measurements [20]. However, a common feature of these measurements is the need to average many repetitions of the measurement, confounding measurements where the dynamics are not identical in every repetition. The presence of thermal noise leads to this nonrepeatability, often resulting in a faster observed decay of an oscillating signal (dephasing). In the present case, inhomogeneous averaging is even more pathological, as thermal fluctuations cause the system to settle into different stable configurations. We are able to disentangle these averaging effects by using a single

nitrogen-vacancy (N-V) spin transition in a nearby diamond nanoparticle as a sensitive magnetometer to read out the final configuration of the vortex following single-shot excitation. As implemented here, this single-spin magnetometry technique has sufficient sensitivity to measure the absolute vortex-core position down to the size of the core itself, approximately 10 nm. With further optimization (narrowing the N-V transition line width and bringing the vortex core closer to the N-V center), significantly better spatial resolution could likely be achieved with this technique. By comparing the time-averaged MOKE data and the single-shot single-spin measurements with a simple model, we can understand the stochastic dynamics of the vortex as it moves in its pinning potential, disentangling effects of inhomogeneous averaging and intrinsic damping. We find that while thermal noise can strongly affect vortex dynamics in a bistable pinning potential, properly

tuned excitation of the vortex can lead to reliable control of the vortex on fast time scales.

## II. THEORY

The ground-state magnetization configuration of a thin ferromagnetic disk with negligible magnetocrystalline anisotropy is a vortex state [21]. The increasing exchange energy cost forces the magnetization at the core of the disk to orient normal to the plane of the disk along  $p\hat{\mathbf{z}}$ , where  $p = \pm 1$  is the polarization of the core. The vortex core is a high-energy-density region that produces a strong localized magnetic fringe field  $\mathbf{B}_v$  above the surface of the disk. Application of an in-plane magnetic field  $\mathbf{B}$  can translate the vortex-core position  $\mathbf{x} = (x, y)$  across the disk [14,22,23]. For small displacements, the rigid vortex model [24] describes the energy of the vortex state:

$$U_0(\mathbf{x}, \mathbf{B}) \approx \frac{1}{2}k|\mathbf{x}|^2 + ck\chi_0(\mathbf{B} \times \mathbf{x}) \cdot \hat{\mathbf{z}}. \quad (1)$$

The first term corresponds to the restoring energy resulting from a balance of the demagnetization and exchange energy, parametrized by a stiffness  $k$ . The second term is the Zeeman energy, which drives the vortex normal to the direction of applied field  $\mathbf{B}$ , where  $c = \pm 1$  indicates the circulation direction of the in-plane magnetization and  $\chi_0$  is the displacement susceptibility. In this case,  $\chi_0 = 104$  nm/mT. In equilibrium, the vortex core follows the path of minimum energy, translating linearly with  $\mathbf{B}$ , where the equilibrium position  $\mathbf{x}_0 = c\chi_0(-B_y, B_x)$  [24,25].

The high energy density and localized structure of the vortex core make it susceptible to pinning at defects in the material or structure of the permalloy disk that lower the energy of the vortex state [17,26]. Pinning sites are included in the model by introducing a pinning potential  $U_p(\mathbf{x}) = -\sum_n w_n(\mathbf{x} - \mathbf{x}_n)$  as a sum of peaked functions  $w_n$  at positions  $\mathbf{x}_n$ . The total energy  $U = U_0 + U_p$  then yields the equilibrium position of the vortex core as it traverses across the disk [17,20].

The nonequilibrium dynamics of the vortex core can be described using Thiele's equation of motion for two-dimensional magnetic vortices [27]:

$$\mathbf{G} \times \dot{\mathbf{x}} - \rho \dot{\mathbf{x}} - \nabla U(\mathbf{x}, \mathbf{B}) = 0, \quad (2)$$

where  $\dot{\mathbf{x}}$  is the time derivative of the vortex-core position,  $\rho$  is a damping factor, and  $\mathbf{G} = -2\pi LM_s \gamma^{-1} p \hat{\mathbf{z}}$  is the gyrotropic vector of a disk with a thickness  $L$ , saturation magnetization  $M_s$ , and gyromagnetic ratio  $\gamma$ . The inertial mass of the vortex core in a micron-sized disk is negligible and therefore any term depending on  $\ddot{\mathbf{x}}$  is ignored [28]. As a result,  $\dot{\mathbf{x}}$  is a function only of the instantaneous position  $\mathbf{x}$  in the potential landscape  $U(\mathbf{x}, \mathbf{B})$  and the subsequent trajectory only depends on the initial position. In the absence of damping, the gyromagnetic force

[the first term in Eq. (2)] is balanced by the restorative force [the third term in Eq. (2)], resulting in a perpetual circulation of the vortex core along an equipotential curve on  $U(\mathbf{x}, \mathbf{B})$  [27,28]. A nonzero  $\rho$  dissipates energy, reducing the amplitude of the vortex-core oscillations over time. With each precession, the energy is reduced by a fraction  $\propto \rho/|\mathbf{G}|$  as it spirals in toward a stable minimum of  $U(\mathbf{x}, \mathbf{B})$ .

## III. SAMPLES AND METHODS

Vortex states are prepared in permalloy ( $\text{Ni}_{0.89}\text{Fe}_{0.19}$ ) disks with a diameter  $D = 2 \mu\text{m}$  and thickness  $L = 40$  nm. The samples are fabricated via electron-beam lithography, electron-beam evaporation, and lift off atop a gold coplanar waveguide (CPW). Diamond nanoparticles (DNPs, DiaScience, Quantum Particles), with a diameter of approximately 25 nm, each containing zero to several N-Vs, are mixed with a 1.0% solution of polyvinyl alcohol,  $M_w = 85\,000$ – $124\,000$  (Aldrich 363146) in deionized water. The DNP solution is spin-coated onto the CPW-permalloy disks, yielding a film thickness of approximately 35 nm. A photoluminescence (PL) map of the N-V-vortex system discussed in this paper is shown in Fig. 1(b). The permalloy disk is outlined in white and the DNP is seen by the bright diffraction-limited PL from several N-V defects.

The measurements are carried out in the following steps. First, we use MOKE to measure the equilibrium displacement of the vortex core while sweeping a magnetic field. This allows us to extract an effective pinning potential along a path through the disk and identify regions of bistable pinning. We then use time-resolved MOKE to measure the (inhomogeneously averaged) dynamics of the vortex as we switch it from one pinning site to another with a magnetic field step. Finally, we apply the same magnetic field step, but then turn it off after a variable delay, using single-spin magnetometry to detect the final equilibrium position of the vortex core.

We measure the equilibrium motion of the vortex core using a differential MOKE technique described in Ref. [29]. We use a continuous-wave laser ( $\lambda = 660$  nm) focused onto the disk through a  $100\times$  oil-immersion objective (NA = 1.25) to measure the equilibrium position of the vortex core. The vortex is offset from the center of the disk toward the DNP by application of an in-plane static field  $B_0 = -2.80$  mT produced by a permanent magnet. We then sweep a magnetic field  $B_1$ , moving the vortex core along the path illustrated in Fig. 1(b) (dotted red line). The relative displacement of the vortex core  $\Delta x_0$  is shown in Fig. 1(c), where  $\Delta x_0^+$  and  $\Delta x_0^-$  correspond to ascending and descending  $B_1$ , respectively. There is a linear trend to  $\Delta x_0$ , corresponding to the equilibrium position of the unpinned energy  $U_0(\mathbf{x})$ . Plateaus and jumps in  $\Delta x_0$  are a result of the vortex core transitioning through the various local minima produced by the pinning potential

$U_p(\mathbf{x})$ . From Fig. 1(c), we can construct an effective one-dimensional pinning potential  $u_p(x)$  (see Ref. [20]), shown in Fig. 1(d). A simulation of  $\Delta x_0$  in the presence of  $u_p$  is included in the inset [the axes are the same as in Fig. 1(c)], demonstrating that  $u_p$  reproduces the observed displacement in response to  $B_1$ .

The pinning landscape produces regions of bistability: fields where there exist multiple local minima of  $U(\mathbf{x})$  and the position of the vortex core is dependent on the path taken to arrive there. For example, fields  $B_\alpha$  and  $B_\beta$  indicated in Fig. 1(c) are within a bistable region produced by the two large pinning sites labeled I and II. These pinning sites likely arise from approximately 10-nm-high bumps on the underlying gold [20]. Smaller pinning sites arising from intrinsic defects in the permalloy are less likely to show clear bistability. Approaching sites I and II from ascending  $B_1$ , the vortex rests at an equilibrium position  $\Delta x_0 = -170$  nm (Site I); whereas approaching from descending  $B_1$ , the vortex rests at  $\Delta x_0 = -65$  nm (site II). To switch the vortex into site I (II), we can apply a magnetic field  $B_I$  ( $B_{II}$ ) outside of the bistable region, where the only potential minimum is at site I (II) [see Fig. 1(c)]. We will now focus on the dynamics of the vortex as it switches between these two pinning sites.

To measure the dynamics of the vortex core, we use a time-resolved differential MOKE technique [15]. A filtered supercontinuum fiber laser produces an optical probe pulse train with a repetition frequency of 3.9 MHz, center wavelength  $\lambda = 660$  nm, and line width  $\sigma = 10$  nm. A digital delay generator (DDG) is synchronized with the optical pulse train to drive a current through the CPW, producing a time-dependent magnetic field  $B_1(t)$ . We measure the longitudinal Kerr rotation of the probe beam as a function of the time delay  $t_d$  between the optical and electrical pulses, yielding  $\Delta x(t_d)$ . In Fig. 1(e), we plot  $\Delta x(t_d)$  in response to a field step. At  $t_d = -140$  ns, the vortex is initialized at  $B_I$  into site I and allowed to relax over a period of 110 ns; at  $t = -30$  ns, the field is returned to  $B_\alpha$ . At  $t_d = 0$  ns, the field is stepped from  $B_\alpha$  to  $B_{II}$  with a rise time of about 1 ns, exciting the gyrotropic motion of the vortex core. As the oscillations of the vortex core decay, the core settles into site II at an equilibrium position  $\Delta x_0 = -65$  nm. We fit the data in Fig. 1(e) to a decaying sinusoidal function  $\Delta x(t_d) = C \sin(2\pi f_g t_d + \phi_0) e^{-t_d/\tau} + x_0$  and find that the vortex oscillates with a frequency  $f_g = 134.6 \pm 0.2$  MHz and decays with a relaxation time  $\tau = 29 \pm 2$  ns.

The N- $V$  spins located in the DNP shown in Fig. 1(b) are initialized and read out via a standard optically detected magnetic resonance (ODMR) technique at room temperature [30,31]. Using the same microscopy setup as the MOKE measurements, the DNPs are illuminated with a CW laser with  $\lambda = 532$  nm exciting the N- $V$  spins and producing a broad PL spectrum centered around 650 nm. The PL is collected by the microscope objective and filtered by a pair of longpass filters with cutoff wavelengths

$\lambda = 550$  nm. The PL is collected by an avalanche photodiode detector (Micro Photon Devices, PDM-50ct), which is connected to a time-correlated single-photon counter (Picoquant Hydraharp 400). A PL image can be obtained by raster scanning the sample stage while collecting photon counts, as in Fig. 1(b). A microwave current is added to the CPW at a frequency  $f_{MW}$  to drive population transfer in the ground state of the N- $V$  center. The PL contrast is measured as the ratio of counts with the microwave current on and off.  $f_{MW}$  is swept as the PL contrast is measured, producing the ODMR spectrum. A reduction in the PL reveals a transition from the  $m_s = 0$  to the  $m_s = \pm 1$  sublevels of the N- $V$  ground state. The net magnetic field  $\mathbf{B}_{net} = \mathbf{B}_0 + \mathbf{B}_1 + \mathbf{B}_v$  at the N- $V$  position results in a splitting between the  $m_s = 0$  and  $m_s = \pm 1$  states  $\nu_{\mp 1} = D_{gs} \pm g\mu_B \mathbf{B}_{net} \cdot \hat{w}$ , where  $D_{gs} = 2.87$  GHz is the zero-field splitting and  $g\mu_B = 28$  GHz/T, and  $\hat{w}$  is oriented along the N- $V$  axis. Shifts of  $\nu_{\mp 1}$  therefore provide a measurement of the unknown  $\mathbf{B}_v$ .

The N- $V$ -spin magnetometer provides more than enough sensitivity to detect the approximately 100 nm difference in vortex-core position between pinning sites I and II [18]. Figure 2(a) shows two ODMR scans taken at an equilibrium field of  $B_\alpha$ , arrived at via an ascending field (blue) or a descending field (red). When approaching  $B_\alpha$  from below, the vortex is trapped in pinning site I and we observe a resonance at  $f_I = 2.61$  GHz. When approaching  $B_\alpha$  from above, the vortex is trapped in pinning site II and the resulting change in  $\mathbf{B}_v$  shifts the resonance outside of the displayed scan range to  $f_{II} = 2.81$  GHz. By measuring ODMR at  $f_I$ , we can easily detect the equilibrium position of the vortex core.

Using the N- $V$  as a readout of the vortex equilibrium position, we can measure the probability  $P$  of switching between pinning sites following a magnetic field pulse. Figures 2(b) and 2(c) illustrate how the measurement is carried out. Starting from the equilibrium applied field where the pinning sites are bistable, a pulse steps the field to  $B_I$  ( $B_{II}$ ) so that site I (II) is the only stable equilibrium, for time  $t_p$ . Starting from bistable field  $B_\alpha$ , for example, a pulse to  $B_I$  for  $t_p = 1$   $\mu$ s reliably initializes the vortex into site I. A subsequent ODMR measurement shows a resonance at  $f_I$ . A pulse to  $B_{II}$  for  $t_p = 50$  ns then attempts to switch the vortex into site II. If it is successful, then no ODMR signal is observed at  $f_I$ . We apply a sequence of these pulses to  $B_I$  and  $B_{II}$ , repeated  $N = 100$  times each. Figure 2(b) shows the result of a 3 s ODMR measurement following each pulse. The resulting data points show two distinct levels, as seen in the histogram in Fig. 2(c). We can then choose a threshold  $O$  between the two well-separated peaks, illustrated by a red dashed line, which delineates an unsuccessful or successful switch into pinning site II from site I. A successful switch is defined by  $s_n = 1$  when the ODMR signal  $> O$ , or  $s_n = 0$  otherwise. We then average over all attempts to obtain  $P(t_p) = 1/N \sum_{n=1}^N s_n$ .

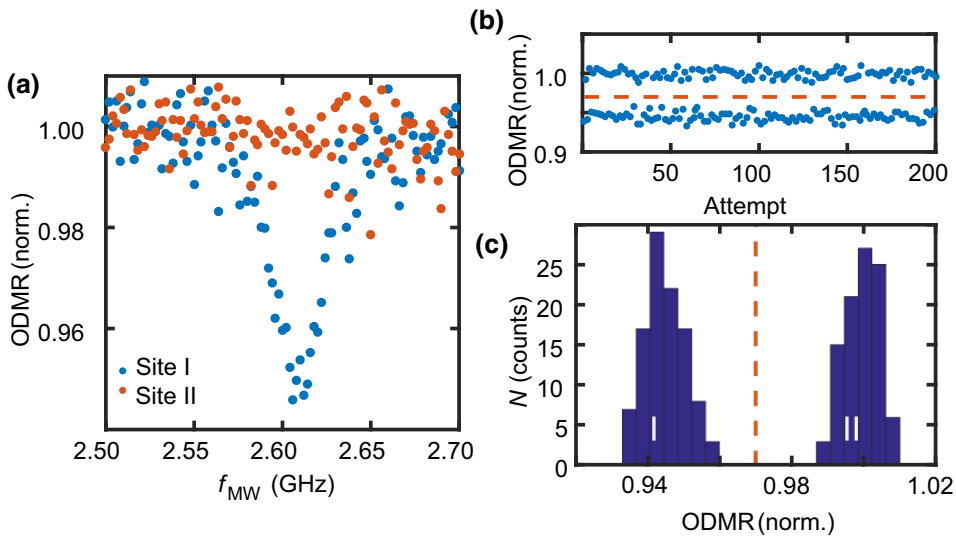


FIG. 2. (a) The ODMR contrast vs  $f_{MW}$  at  $B_\alpha$  approaching with an ascending field (blue) and a descending field (red), causing the vortex to settle into pinning site I and II, respectively. (b) The ODMR contrast at  $f_{MW} = 2.61$  GHz following sequential  $B_I$  and  $B_{II}$  pulses for  $N = 100$  switches. (c) The histogram of the ODMR contrast data in (b): the threshold  $O$  separating data sets I and II is illustrated by a red dashed line.

#### IV. RESULTS

Using this method, we now explore how  $P$  depends on the applied pulse characteristics. By adjusting the static magnetic field, we can adjust the relative stability of sites I and II. We consider two cases: sites I and II of roughly equal stability (configuration  $\alpha$ ) and site II less stable than site I (configuration  $\beta$ ). The blue curve in Fig. 3(a) shows the potential for configuration  $\alpha$ . At this magnetic field ( $B_\alpha$ ), there are two local minima with similar depths and widths. By decreasing the magnetic field to  $B_\beta$ , the potential is tilted toward site I, making site I more stable and site II less stable, as shown in blue in Fig. 3(b). Here, site I is now deeper and site II is barely still a stable minimum. From these static fields, we apply a pulse to  $B_{II}$  for a time  $t_p$ . This pulse tilts the potential toward site II sufficiently that site II is the only stable minimum in the pinning potential [Figs. 3(a) and 3(b), red]. We now perform the measurement outlined in Fig. 2 at different  $t_p$ , constructing  $P(t_p)$  for the two cases.

The switching probability  $P(t_p)$  for configuration  $\alpha$  is shown in Fig. 3(c). At a short pulse length ( $t_p < 4$  ns),  $P = 0$ , because the pulse is not long enough to break the vortex free from site I. At a sufficiently long pulse length ( $t_p > 45$  ns), the system has enough time to relax into site II and  $P = 1$ . In the intermediate regime, fast oscillations of  $P$  are observed with  $t_p$ . The same measurement is carried out 48 h later [Fig. 3(c), red], demonstrating that these oscillations are stable and repeatable. At  $t_p < 22$  ns, the oscillations show a general upward trend and at  $t_p > 22$  ns, the peaks of the oscillations begin to saturate at  $P = 1$ . The red dots in Fig. 3(c) show multiples of  $1/f_g$ , highlighting good agreement between the measured gyrotropic period and the oscillations in  $P$  at larger  $t_p$ . Intriguingly, the saturation of the oscillations suggests that reliable switching can be achieved with pulses faster than the vortex's relaxation time.

For configuration  $\beta$  [Fig. 3(d)],  $P$  shows a gradual rise from zero to near unity, with only small oscillations observed in between. Here, the saturation of  $P$  does not occur until  $t_p \approx 75$  ns. Even after the vortex has relaxed into site II at these long pulse times, there is still a finite probability that the vortex will escape back into site I when the pulse ends, preventing saturation at  $P = 1$ .

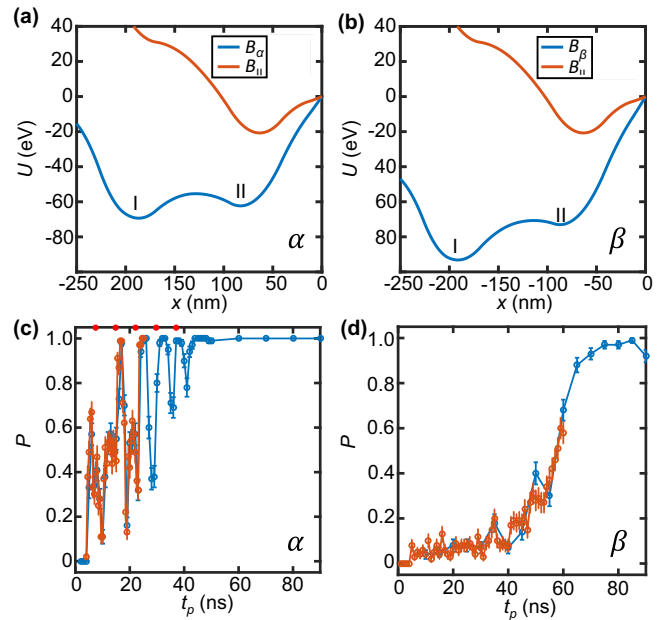


FIG. 3. (a),(b) The total potential  $U_0 + u_p$  at the switching fields  $B_I$  (red) and the bistable fields  $B_\alpha$  and  $B_\beta$  (blue), respectively, constituting configurations  $\alpha$  and  $\beta$ . (c),(d) The probability  $P$  of switching from site I to II in response to a  $B_{II}$  pulse vs the pulse length  $t_p$  for configurations  $\alpha$  and  $\beta$ , respectively. Initial measurements are shown in blue: after 48 h, the measurements shown in red are performed to demonstrate repeatability. Red dots in (c) indicate multiples of  $1/f_g$ .

## V. ANALYSIS AND DISCUSSION

To understand the measured  $P(t_p)$ , we simulate the vortex dynamics by numerically solving Eq. (2) using the Matlab ordinary differential equation (ODE) solver. The two-dimensional pinning potential  $U_p(\mathbf{x})$  is constructed by approximating pinning sites I and II as symmetric Gaussian wells with similar depths and widths to those found in the effective one-dimensional pinning potential  $u_p(x)$  [Fig. 1(d)]. The simulation parameters are set to match the geometrical, material, and physical constants observed in the experiment. A 1 ns rise time is included in the field-pulse profiles used in the simulations.

The red curve in Fig. 4(a) shows the calculated trajectory  $\mathbf{x}_d(t)$  of the vortex core following a step from  $B_\alpha$  to  $B_{II}$ . The trajectory starts at the initial equilibrium position in pinning site I ( $x = -175$  nm) and displays the typical damped spiraling motion, settling into the new equilibrium

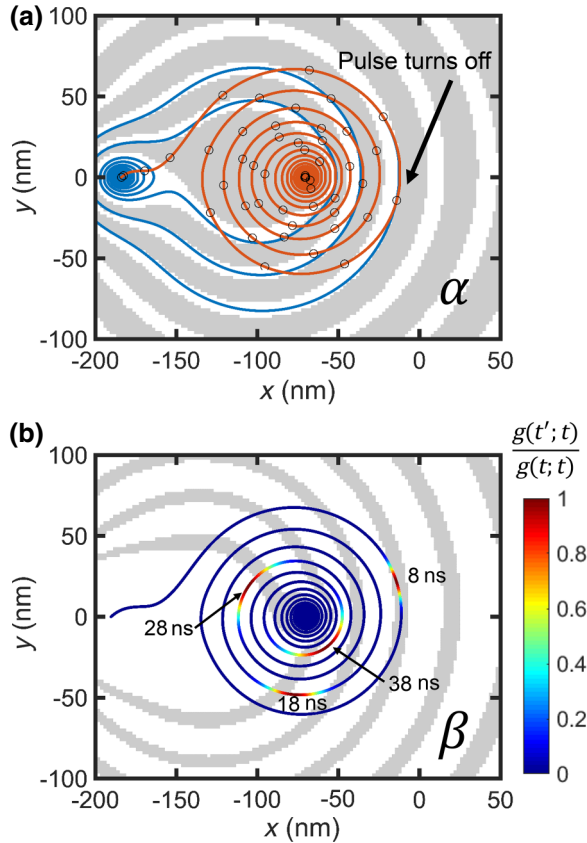


FIG. 4. (a) The basins-of-attraction map  $S(\mathbf{x}_0)$  for configuration  $\alpha$  (gray,  $S = 1$ ; white,  $S = 0$ ). The deterministic path  $\mathbf{x}_d(t)$  (red) is shown in response to a field step from  $B_\alpha$  to  $B_{II}$ . The markers along  $\mathbf{x}_d(t)$  represent 1 ns intervals. The blue curve shows the subsequent trajectory after the field has been reduced back to  $B_\alpha$  at  $t = 9$  ns. (b)  $S(\mathbf{x}_0)$  for configuration  $\beta$  and  $\mathbf{x}_d(t)$  in response to a field step from  $B_\beta$  to  $B_{II}$  with a color scale  $g(t'; t)/g(t; t)$  at various  $t$ .

in site II. In the switching experiment, the vortex core would travel along this trajectory for a time  $t_p$ , at which point the pulse would end. Then, from a position  $\mathbf{x}_0$  somewhere along the red curve, the dynamics would evolve in the bistable potential, relaxing into either site I or II. For example, the blue curve shows the evolution of the vortex into site I after returning the field to  $B_\alpha$  at  $t = 9$  ns.

Whether the vortex relaxes into site I or II in the bistable potential depends only on the position  $\mathbf{x}_0$  when the pulse is turned off. As a result, we can map out the final pinning site as a function of  $\mathbf{x}_0$ . This map, the “basins of attraction”  $S(\mathbf{x})$ , is calculated by initializing the vortex to some position  $\mathbf{x}_0$  and allowing it to evolve according to Eq. (2), eventually settling into either pinning site I or II. If, for a given  $\mathbf{x}_0$ , the vortex settles into pinning site I, then  $S(\mathbf{x}_0) = 0$ . If instead, the vortex settles into pinning site II, then  $S(\mathbf{x}_0) = 1$ . Then by sweeping  $\mathbf{x}_0$  we construct  $S(\mathbf{x})$  shown in Fig. 4(a) at  $B_\alpha$ , with  $S(\mathbf{x}_0) = 0$  (1) colored white (gray). The two basins are characterized by spirals centered around the two pinning sites where the basins are the largest. The basins of attraction at  $B_\beta$  are similar, but with site I’s basin now covering a greater area than that of site II [Fig. 4(b)]. The area of the central basins and the widths of the spiral arms are directly related to the stability of the corresponding pinning site.

Through the combination of the trajectory  $\mathbf{x}_d(t)$  during the pulse and the basins-of-attraction map for the bistable potential, we can roughly understand the behavior of  $P$ . As  $\mathbf{x}_d(t_p)$  cuts through different basins, the final vortex position alternates between sites I and II. At sufficiently large  $t_p$ ,  $\mathbf{x}_d(t_p)$  is entirely contained within the basin for site II, yielding constant  $P = 1$ . Unlike the observed behavior, however, this zero-temperature model predicts deterministic behavior with  $P = 0$  or 1.

Next, we consider the effects of thermal noise on the dynamics of the vortex core. In previous work [32], the dynamics of the vortex in a bistable potential in the presence of thermal noise was studied by adding a stochastic noise term to Eq. (2) and solving numerically. The behavior of  $P$  calculated in that work agreed qualitatively with the results here. To compare with our experimental results, we draw on those results to construct a simpler effective model.

To account for thermal effects in our model, we assume that the vortex-core position  $\mathbf{x}(t)$  diffuses away from the deterministic position  $\mathbf{x}_d(t)$ . In the stochastic simulations in Ref. [32], it was observed that this diffusion mainly occurs tangential to  $\mathbf{x}_d(t)$ , as opposed to the perpendicular directions. We therefore take  $\mathbf{x}(t) = \mathbf{x}_d(t')$ , with  $t'$  drawn from a continuous Gaussian probability distribution  $g(t'; t)$  centered at  $t$ . The width of  $g(t'; t)$  is parametrized by  $\sigma(t) = D\sqrt{t}$ , where the diffusion constant  $D$  sets the amplitude of dephasing. The spreading of  $\mathbf{x}(t)$  is shown for several values of  $t$  along  $\mathbf{x}_d(t)$  for a pulse from  $B_\beta$  to  $B_{II}$  in Fig. 4(b).

We can now calculate the probability of settling into pinning site II as the average of basins  $P(t) = \langle S(\mathbf{x}(t)) \rangle = \int_0^\infty S(\mathbf{x}_d(t'))g(t'; t)dt'$ . The waveform generator used is subject to 0.2 ns of jitter in the pulses produced. To account for this, we perform a convolution of  $P$  with a normalized Gaussian that has a full width at half maximum  $F = 0.2$  ns. We can also calculate the average position  $\langle \mathbf{x}(t) \rangle = \int_0^\infty \mathbf{x}_d(t')g(t'; t)dt'$ . The decay time observed in  $\langle \mathbf{x} \rangle$  results from a combination of damping and dephasing, set by the parameters  $\rho$  and  $D$ , respectively.

As is typical for pump-probe measurements, the observed decay of the time-resolved MOKE signal does not uniquely determine the contributions from  $\rho$  and  $D$ . In Fig. 5(a), we plot the measured  $\Delta x_0$  (circles), along with the calculated  $\langle x \rangle$  with four different pairs of values for  $\rho$  and  $D$ . These values range from low dephasing and high damping ( $\rho/|\mathbf{G}| = 0.04$  and  $D = 0.01\sqrt{ns}$ ) to high dephasing and low damping ( $\rho/|\mathbf{G}| = 0.02$  and  $D = 0.21\sqrt{ns}$ ). Because  $\sigma$  has units of time,  $D$  has units of square root of time. Each calculated curve reasonably matches the observed decay time. (Shifts in the frequency at long times arise from the details of the pinning potential.) As we will see below, however, the switching data  $P(t_p)$  do depend on the choice of these parameters, allowing us to disentangle the effects of damping and dephasing.

Figures 5(b)–5(i) show the calculated  $P(t_p)$  for the four sets of  $\rho$  and  $D$ . The left column corresponds to configuration  $\alpha$  and the right column to configuration  $\beta$ . In both cases, low  $D$  results in fast sharp oscillations in  $P(t_p)$  going all the way to one and/or zero. In the limit of low  $D$ , the vortex does not spread out along the deterministic trajectory  $\mathbf{x}_d(t)$ , with  $P$  showing a sharp transition each time  $\mathbf{x}_d(t)$  crosses a basin boundary. At  $t_p > 40$  ns,  $\mathbf{x}_d$  lies entirely inside the basin for site II, so  $P = 1$ . In the high-dephasing regime, Figs. 5(e) and 5(i), the trajectory spreads out quickly along  $\mathbf{x}_d(t)$ , largely smearing out the fast fluctuations in  $P(t_p)$ . Particularly at longer  $t_p$ ,  $P$  rises smoothly, not attaining  $P = 1$  until the trailing tail of the distribution has entered site II's basin, around  $t_p = 75$  ns.

The intermediate values of  $\rho$  and  $D$  yield the best match with the experimental results. For configuration  $\alpha$ , the calculated  $P$  in Fig. 5(c) shows the same characteristics as the measured result. At  $t_p < 5$  ns, we see  $P(t_p) = 0$  due to insufficient time for the vortex to escape pinning site I. At sufficiently long  $t_p > 40$  ns,  $P(t_p) = 1$  when the distribution along  $\mathbf{x}_d$  is completely contained by the basin of site II. Between  $t_p = 5$  ns and  $t_p = 20$  ns, we observe significant oscillations in  $P(t_p)$ , though not as large or rapid as in the low- $D$  case. Here, the fastest oscillations, where  $\mathbf{x}_d$  rapidly cuts across basins, are smeared out. On the other hand, regions where  $\mathbf{x}_d(t)$  lies within a single basin for an extended range still can result in significant oscillations of  $P$ . This can happen at multiples of  $1/f_g$  or  $1/2f_g$  where the curvature of  $\mathbf{x}_d(t)$  most closely matches the curvature of the spirals in  $S(\mathbf{x})$  or where  $\mathbf{x}_d(t)$  crosses the

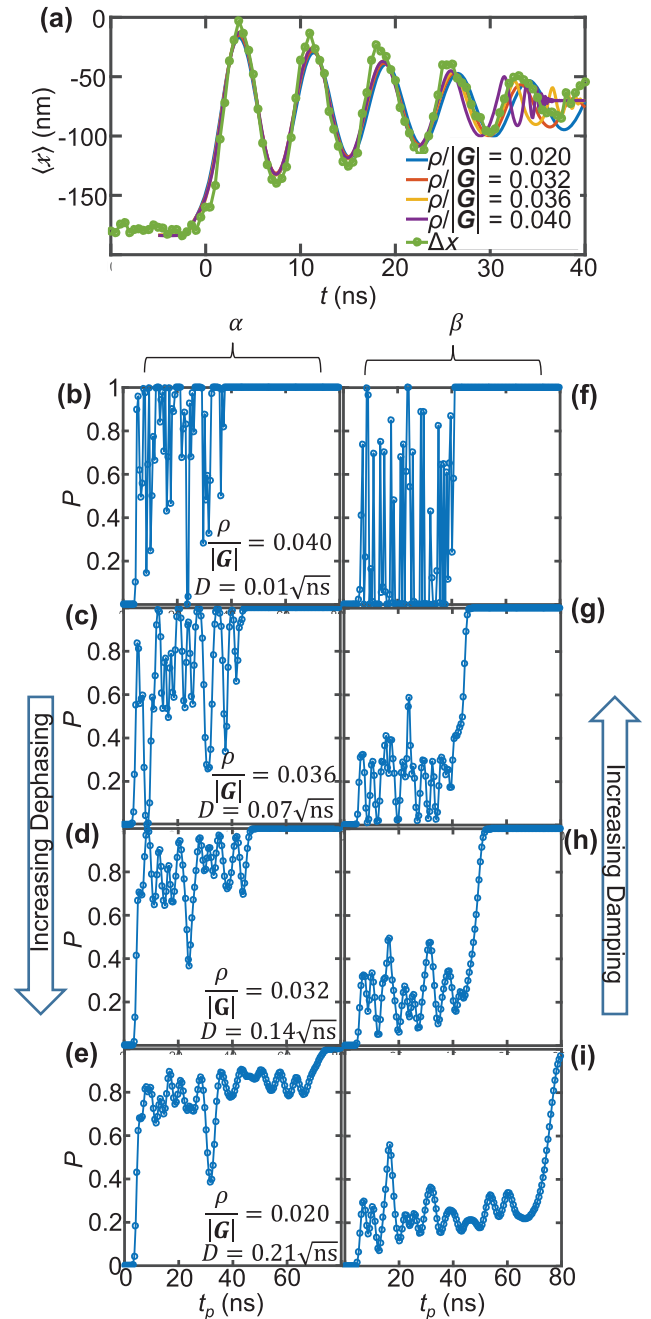


FIG. 5. (a) A plot of the calculated average  $x$  position  $\langle x \rangle$  of the vortex core for the parameters in (b)–(i), along with the experimentally measured position  $\Delta x_0$ . (b)–(i) Plots of the calculated probability  $P$  of switching from pinning site I to II vs pulse length  $t_p$  with varying damping ( $\rho$ ) and dephasing ( $D$ ) parameters: (b)–(e)  $P$  for configuration  $\alpha$ ; (f)–(i)  $P$  for configuration  $\beta$ .

large central basin. At  $t_p > 20$  ns, we observe the peaks of the oscillations beginning to saturate at  $P = 1$ , as the distribution along  $\mathbf{x}_d$  becomes almost entirely contained within site II's central basin along part of its trajectory. In configuration  $\beta$ , we see reasonable agreement between the experiment and the simulation in Fig. 5(h). In general,

we observe a suppression of  $P(t_p)$  prior to the rise up to saturation. This suppression occurs because of a reduction in area of basin B relative to basin A, as seen in Fig. 4(b). As a result, the distribution along  $\mathbf{x}_d$  is never fully encompassed by a region of basin B and  $P(t_p)$  remains low. As in the experiment, we observe a rise in  $P$  up to saturation as the distribution fully enters the central basin.

For proposed devices that rely on translation of a magnetic vortex at room temperature, quick and reliable control of the vortex core is necessary. In the presence of pinning, this control is nontrivial, particularly in the case of bistable pinning sites. By combining inhomogeneously averaged time-resolved MOKE microscopy with single-shot spin-based readout of the final vortex position, we can both characterize the pinning potential seen by the vortex and understand the stochastic vortex-core dynamics as it switches between adjacent bistable pinning sites. These experimental techniques, in conjunction with the model presented here, yield an approach to the engineering of fast controllable dynamics of vortices or other nanoscale magnetic textures in a complex pinning landscape.

#### ACKNOWLEDGMENTS

This work was supported by DOE Grant No. DESC008148.

- 
- [1] A. Imre, G. Csaba, L. Ji, A. Orlov, G. Bernstein, and W. Porod, Majority logic gate for magnetic quantum-dot cellular automata, *Science* **311**, 205 (2006).
- [2] S. Parkin, M. Hayashi, and L. Thomas, Magnetic domain-wall racetrack memory, *Science* **320**, 190 (2008).
- [3] D. Allwood, G. Xiong, M. Cooke, C. Faulkner, D. Atkinson, N. Vernier, and R. Cowburn, Submicrometer ferromagnetic Not gate and shift register, *Science* **296**, 2003 (2002).
- [4] D. Allwood, G. Xiong, C. Faulkner, D. Atkinson, D. Petit, and R. Cowburn, Magnetic domain-wall logic, *Science* **309**, 1688 (2005).
- [5] A. Fert, V. Cros, and J. Sampaio, Skyrmions on the track, *Nat. Nanotechnol.* **8**, 152 (2013).
- [6] S. Sugimoto, Y. Fukuma, S. Kasai, T. Kimura, A. Barman, and Y. Otani, Dynamics of Coupled Vortices in a Pair of Ferromagnetic Disks, *Phys. Rev. Lett.* **106**, 197203 (2011).
- [7] H. Jung, K. Lee, D. Jeong, Y. Choi, Y. Yu, D. Han, A. Vogel, L. Bocklage, G. Meier, M. Im, P. Fischer, and S. Kim, Tunable negligible-loss energy transfer between dipolar-coupled magnetic disks by stimulated vortex gyration, *Sci. Rep.* **1**, 59 (2011).
- [8] M. Rahm, J. Stahl, and D. Weiss, Programmable logic elements based on ferromagnetic nanodisks containing two antidots, *Appl. Phys. Lett.* **87**, 182107 (2005).
- [9] A. Dussaux, B. Georges, J. Grollier, C. Cros, A. Khvalkovskiy, A. Fukushima, M. Konoto, H. Kubota, K. Yakushiji, S. Yuasa, K. Zvezdin, K. Ando, and A. Fert, Large microwave generation from current-driven magnetic vortex oscillators in magnetic tunnel junctions, *Nat. Commun.* **1**, 8 (2010).
- [10] J. Fried and P. Metaxas, Nanoparticle-modified magnetic vortex dynamics, *IEEE Magn. Lett.* **8**, 4105205 (2017).
- [11] C. Serpico, M. D'Aquino, G. Bertotti, and I. D. Mayergoyz, Analytical description of quasi-random magnetization relaxation to equilibrium, *IEEE Trans. Magn.* **45**, 5224 (2009).
- [12] S. Kaka and S. E. Russek, Precessional switching of submicrometer spin valves, *Appl. Phys. Lett.* **80**, 2958 (2002).
- [13] S. Pollard, L. Huang, K. Buchanan, D. Arena, and Z. Y. Direct dynamic imaging of non-adiabatic spin torque effects, *Nat. Commun.* **3**, 1028 (2012).
- [14] R. Cowburn, D. Koltsov, A. Adeyeye, M. Welland, and D. Tricker, Single-Domain Circular Nanomagnets, *Phys. Rev. Lett.* **83**, 1042 (1999).
- [15] R. Badea and J. Berezovsky, Dynamically controlled energy dissipation for fast magnetic vortex switching, *J. Appl. Phys.* **122**, 093904 (2017).
- [16] T. Chen, A. Galkiewicz, and P. Crowell, Phase diagram of magnetic vortex dynamics, *Phys. Rev. B* **85**, 180406 (2012).
- [17] J. Burgess, A. Fraser, F. Sani, D. Vick, B. Hauer, J. Davis, and M. Freeman, Quantitative magneto-mechanical detection and control of the Barkhausen effect, *Science* **339**, 1051 (2013).
- [18] R. Badea, M. Wolf, and J. Berezovsky, Exploiting bistable pinning of a ferromagnetic vortex for nitrogen-vacancy spin control, *Appl. Phys. Lett.* **109**, 132403 (2016).
- [19] B. V. Waeyenberge, A. Puzic, H. Stoll, K. Chou, T. Tylliszczak, R. Hertel, M. Fähnle, H. Brückl, K. Rott, G. Reiss, I. Neudecker, D. Weiss, C. Back, and G. Schütz, Magnetic vortex core reversal by excitation with short bursts of an alternating field, *Nature* **444**, 461 (2006).
- [20] R. Badea and J. Berezovsky, Mapping the Landscape of Domain-Wall Pinning in Ferromagnetic Films Using Differential Magneto-Optical Microscopy, *Phys. Rev. Appl.* **5**, 064003 (2016).
- [21] T. Shinjo, T. Okuno, R. Hassdorf, K. Shigeto, and T. Ono, Magnetic vortex core observation in circular dots of permalloy, *Science* **289**, 930 (2000).
- [22] A. Wachowiak, J. Wiebe, M. Bode, O. Pietzsch, M. Morgenstern, and R. Wiesendanger, Direct observation of internal spin structure of magnetic vortex cores, *Science* **298**, 577 (2002).
- [23] R. Höllinger, A. Killinger, and U. Krey, Statics and fast dynamics of nanomagnets with vortex structure, *J. Magn. Mater.* **261**, 178 (2003).
- [24] K. Guslienko, V. Novosad, Y. Otani, H. Shima, and K. Fukamichi, Field evolution of magnetic vortex state in ferromagnetic disks, *Appl. Phys. Lett.* **78**, 3848 (2001).
- [25] J. Burgess, J. Losby, and M. Freeman, An analytical model for vortex core pinning in a micromagnetic disk, *J. Magn. Mater.* **361**, 140 (2014).
- [26] H. Barkhausen, *Phys. Z.* **20**, 401 (1916).
- [27] A. Thiele, Steady-State Motion of Magnetic Domains, *Phys. Rev. Lett.* **30**, 230 (1973).
- [28] K. Guslienko, B. Ivanov, V. Novosad, Y. Otani, H. Shima, and K. Kukamichi, Eigenfrequencies of vortex state excitations in magnetic submicron-size disks, *J. Appl. Phys.* **91**, 8037 (2002).



- [29] R. Badea, J. Frey, and J. Berezovsky, Magneto-optical imaging of vortex domain deformation in pinning sites, *J. Magn. Magn. Mater.* **381**, 469 (2015).
- [30] P. Neumann, R. Kolesov, V. Jaques, J. Beck, J. Tisler, A. Batalov, L. Rogers, N. Manson, G. Balasubramanian, and F. Jelezko, Excited-state spectroscopy of single NV defects in diamond using optically detected magnetic resonance, *New J. Phys.* **11**, 1 (2009).
- [31] M. Wolf, R. Badea, and J. Berezovsky, Fast nanoscale addressability of nitrogen-vacancy spins via coupling to a dynamic ferromagnetic vortex, *Nat. Commun.* **7**, 11584 (2016).
- [32] E. Haber, R. Badea, and J. Berezovsky, Simulating the room-temperature dynamic motion of a ferromagnetic vortex in a bistable potential, *J. Magn. Magn. Mater.* **454**, 289 (2018).